Atmos. Chem. Phys., 11, 13201–13217, 2011
www.atmos-chem-phys.net/11/13201/2011/
doi:10.5194/acp-11-13201-2011

Atmospheric Chemistry and Physics

Analyzing coastal precipitation using TRMM observations

R. H. Heiblum, I. Koren, and O. Altaratz

Department of Environmental Sciences, Weizmann Institute, Rehovot, Israel

Received: 5 April 2011 – Published in Atmos. Chem. Phys. Discuss.: 23 May 2011
Revised: 11 December 2011 – Accepted: 12 December 2011 – Published: 21 December 2011

Abstract. The interaction between breezes and synoptic gradient winds, and surface friction increase in transition from sea to land can create persistent convergence zones nearby coastlines. The low level convergence of moist air promotes the dynamical and microphysical processes responsible for the formation of clouds and precipitation.

Our work focuses on the winter seasons of 1998–2011 in the Eastern Mediterranean. During the winter the Mediterranean sea is usually warmer than the adjacent land, resulting in frequent occurrence of land breeze that opposes the common synoptic winds. Using rain-rate vertical profiles from the Tropical Rainfall Measurement Mission (TRMM) satellite, we examined the spatial and temporal distribution of average hydrometeor mass in clouds as a function of the distance from coastlines.

Results show that coastlines in the Eastern Mediterranean are indeed favored areas for precipitation formation. The intra-seasonal and diurnal changes in the distribution of hydrometeor mass indicate that the land breeze may likely be the main responsible mechanism behind our results.

1 Introduction

The global hydrological cycle is of great importance to our wellbeing. Understanding this cycle is crucial when dealing with water resources management, agriculture, global demographics and politics. Precipitation processes play a key component in the hydrological cycle. Although 75 %–80 % of global precipitation occurs over oceans (see http://ww2010.atmos.uiuc.edu/(Gh)/guides/mtr/hyd/bdgt.rxml) the precipitation-evaporation budget is positive over land and negative over oceans, making precipitation our main source of fresh water. Additionally, the latent heat released in precipitation processes is a major driver of the global atmospheric circulation, and hence affects climate variations around the globe (Trenberth et al., 2009). Understanding the dynamic and microphysical processes behind precipitation formation is of great importance in semi-arid climate regions which are especially sensitive to rainfall variations, such as the Eastern Mediterranean (EM), South Western US and Eastern Africa. Moreover, due to their highly non-linear nature, precipitation processes (especially cold rain processes) are still far from being resolved and our current understanding is limited (Levin and Cotton, 2009)

In this work we examine coastal precipitation formation, explained by combined effects of synoptic winds, land breeze, surface friction and orographic forcing as major contributors for mesoscale convergence, in both meteorological and climatological time scales.

1.1 Previous studies

Sea breeze (SB) and Land breeze (LB) are basically the same physical effect but with opposite temperature gradients (Schmidt, 1947; Fisher, 1960, 1961). In the SB case, a local cool and dense air mass forms over a water body, and creates a flow towards the hotter, lighter inland air mass. The LB is exactly opposite, with the denser, cooler air originating over land. The SB and LB breezes are confined mainly up to heights of 1–1.5 km, which corresponds to the boundary layer of the atmosphere. An analytical analysis (Schmidt, 1947) showed the thermally induced SB to be a stronger effect than LB, but this of course depends on local, low level temperature distributions over sea and land during day and night, and may vary from one location to another. Moreover, for both SB and LB, the vertical profiles of horizontal winds contain an upper level return flow opposed to the low level flow as expected from continuity considerations.

Correspondence to: I. Koren
(ilan.koren@weizmann.ac.il)

Published by Copernicus Publications on behalf of the European Geosciences Union.

Interaction between breezes and synoptic gradient winds can contribute to low level convergence, and therefore to cloud and precipitation formation. Intergrating the mass conservation equation for incompressible fluids with respect to height, we get:

$$w(D) = \int_0^D \left(\frac{\partial u}{\partial x} + \frac{\partial v}{\partial y} \right) dz \quad (1)$$

where w is the updraft vertical velocity, u is the zonal velocity, v is the meridonial velocity and D is an arbitrary height that can be taken to be the top of the planetary boundary layer. Hence, horizontal convergence of low level winds in the boundary layer result in upward vertical transport (updrafts) of mass and momentum at the top of the layer. In the case of which the level of free convection (LFC) is above a low level inversion layer, these updrafts can break through the inversion, supplying heat and moisture to the upper atmosphere. Furthermore, updraft velocities are proportional to condensation rate of cloud droplets (release of latent heat) and maximum supersaturation, promoting convection processes in the cloud. In convective clouds for instance, supersaturation is proportional to the updraft velocities (Fukuta, 1993).

Theory and simulations show that higher supersaturation/updrafts can increase both diffusional growth rates and coalescence of droplets (Mordy, 1959; Leighton and Rogers, 1974; Rogers and Yau, 1989; Nelson, 1971), which are crucial in the initiation and growth of warm precipitation (involves only liquid water). This is also pronounced in mixed phase clouds, higher supersaturation values of vapor relative to ice (that are higher than relative to water) will create more rapid diffusional ice growth (Stickley, 1940; Byers, 1965). Additionally, stronger updrafts transport more droplets above the freezing level of the cloud, promoting the highly efficient accretion/riming (i.e. growth by coalesence of ice particles and supercooled droplets) processes that initiate cold rain (Houghton, 1950; Ludlam, 1952; Houghton, 1968; Hindman and Johnson, 1972; Reinking, 1975) and later also more efficient aggregation processes.

Observations indeed show that low level convergance promotes cloud convection. Frequent nocturnal thunderstorms (Neumann, 1951) observed near the Eastern Mediterranean coastline were explained by: (i) the convergence of synoptic gradient winds with LB (ii) the convergent effect coastline curvature may play on low level winds, with concave coastlines favoring LB convergence and convex coastlines favoring SB convergence. Similar effects of cloud formation as a result of low level convergence were observed (Purdom, 1976) nearby other land-water interfaces such as rivers and lakes. Furthermore, breeze fronts were seen to interact with preexisting convection lines and thunderstorms, greatly intensifying the mesoscale convection. Radar observations of regions exhibiting LBs opposing gradient winds (Meyer, 1971; Schoenberger, 1984) showed frontal zones of nocturnal cumulus clouds which form nearby coastlines and propagate further offshore at a speed dependent on the temperature difference between the land and sea. These LB fronts usually dissipated after sunrise (i.e. land heating) and were most pronounced when the gradient winds and the LB were of comparable magnitudes. An example for such a LB front is shown in Fig. 1, where a nearly stationary line of precipitating clouds formed off the coast of Israel.

As follows from the thermally driven nature of breezes, their effects are expected to have significant diurnal variability. Java Island in South East Asia is an extreme case for a breeze dominated diurnal precipitation regime (Qian, 2008). The Island is surrounded with warm waters and experiences daytime (nighttime) precipitation concentrated over the land (sea). The high mountain range along the Island's interior produces daytime (nighttime) anabatic (katabatic) winds that flow in phase with the local breeze, intensifying the diurnal cycle.

Orographic forcing is considered to be another strong influence on cloud and precipitation formation (Smith, 1989, 2006; Houze, 1993). Horizontal moist winds that approach a topographic obstacle are forced to rise and cool with a vertical velocity proportional to the horizontal wind velocity and obstacle height gradient. The forced updrafts induce the formation of clouds and precipitation as discussed above. The location of maximum precipitation with respect to the obstacle depends mainly on the ratio between the microphysical processes and advection time scales, and can range from 50 km upwind (e.g. with very weak horizontal winds of $\sim 2\,\mathrm{m\,s^{-1}}$) the peak height location to slightly downwind (Pathirana et al., 2005). Moreover, gravity wave dynamics may create an upwind tilt in the condensation pattern. Generally, most of the precipitation falls on the upslope of the obstacle. The flow reaching the lee-side receives little precipitation due to adiabatic descent (warming) and earlier depletion of moisture. In the case of an unstable, convective atmosphere, topographic obstacles are considered especially efficient in depleting the cloud's water content. In some cases, orographic forcing near coastal areas may combine with local mesoscale breezes and create a coupled effect. A previous study in central Israel (Rosenfeld, 1986) concluded that clouds "feel" the presence of an orographic obstacle 15 km upwind the mean flow, not far from the coastlines.

Another factor that influences coastal precipitation formation is frictional convergence (FC). From basic theory (Wallace and Hobbs, 2006a) we learn that the drag force is proportional to the square of the wind speed and drag coefficient C_D (C_D grows at wind speeds larger than $5\,\mathrm{m\,s^{-1}}$). Therefore, increased surface roughness in transition from sea to land may also play a significant role in low level convergence near coastlines, and especially when the winds are strong. Indeed, numerical studies (Malda et al., 2007; Kimball, 2008) indicate that interactions between the low-level gradient wind and surface can create convergence zones that greatly affect

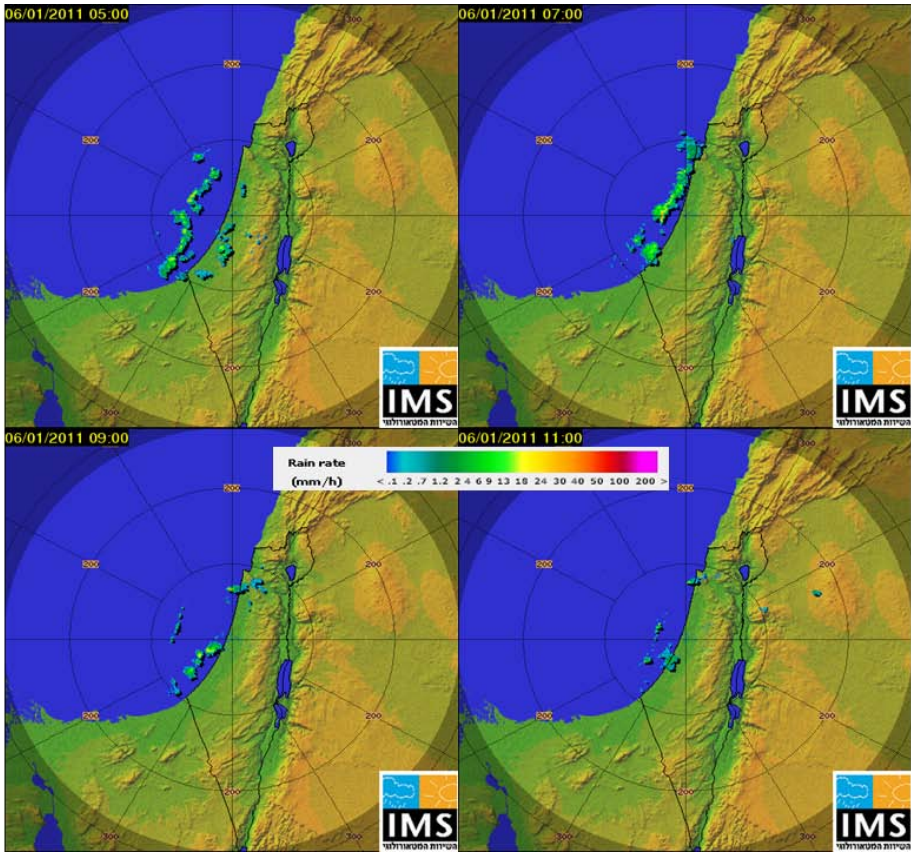

Fig. 1. Radar image evolution of rain clouds off the coast of Israel, 6 January 2011, from 05:00 to 11:00 local time, at two hour intervals. The rain clouds started dissipating after sunrise. The image serves as an example of an almost stationary precipitation line formed offshore, and is likely attributed to an offshore LB front. Image taken from the Israeli Meteorological Service (IMS) website, at http://www.ims.gov.il.

the spatial distribution, intensity and other characteristics of coastal precipitation.

1.2 Eastern Mediterranean

The last IPCC report (Climate Change 2007 Synthesis report, Sects. 3.2, 3.3. Available at: http://www.ipcc.ch/) predicts that the Mediterranean region will experience a hotter and drier climate, among others due to the predicted expansion of the Hadley circulation derived from global warming (Lu et al., 2007). Such climate changes may have devastating implications on water resources for the already water stressed countries in the region. According to Köppen's climate classification (Goldreich, 2003), Mediterranean climates are characterized by hot, dry summers and cold, wet winters with most of the rainfall concentrated in the months D-J-F.

During the Northern Hemisphere winter, the southward drift of the subtropical high enables cold air from Europe to penetrate into the Mediterranean where cold low pressure systems are formed (Alpert et al., 1990a, 1990b). These systems may further intensify through processes of low-level baroclinic instability i.e. large thermal contrast between the sea and cold air to its north and lee cyclogenesis near southern Turkey. Some of these cyclones reach the EM and are called Cyprus lows, acquiring their name from their mean geographic location. The passage of a Cyprus low is dominated by westerly winds along the central part of the Eastern Mediterranean coast (Zangvil and Druian, 1990) and constitutes as the most common synoptic setting under which precipitation develops in the EM, yielding about 90 % of the rainfall in the central and northern parts of Israel (Goldreich, 2003; Saaroni et al., 2010). The common setting of a Cyprus low is shown in Fig. 2, from which it can be seen that the gradient winds tend to flow inland except near western Turkey. Another type of synoptic system that can produce precipitation in the eastern Mediterranean is the "Red Sea Trough". It will not be discussed hereafter due to very low rainfall related to these systems.

During the rainy months studied here (November–March), EM Sea Surface temperatures are usually warmer than the adjacent land by 2–10 °C, making LB a common phenomena during the winter (Neumann, 1951; Goldreich, 2003; Levy et al., 2008). The LB magnitude varies both

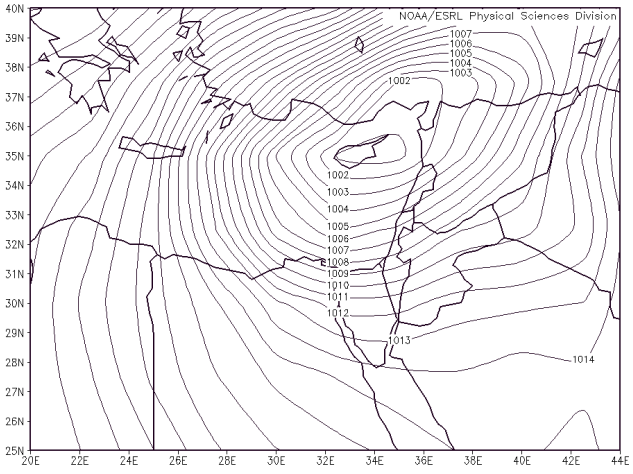

Fig. 2. Typical synoptic setting of Cyprus low in the EM, 29 January 2008. Mean sea level pressure isobars are displayed and labeled in hPa units. Image provided by the NOAA/OAR/ESRL PSD, Boulder, Colorado, USA, from their Web site at http://www.esrl.noaa.gov/psd/.

diurnally: maximum (minimum) Land-Sea Temperature Difference (LSTD) at sunrise (afternoon), and seasonally: maximum (minimum) LSTD during December (March). The cyclones reaching the EM also display significant intra-seasonal variability (Goldreich et al., 2004, 2006; Alpert et al., 1990b). November and December are considered transition months from autumn to winter and experience relatively shallow upper level troughs and weak (shallower) vortices. On the other hand, the period of January till March is characterized by deep upper level troughs and more intense vortices. The EM may be a classic case where the interaction between LB and synoptic winds promotes convection and precipitation formation, because most of the rain in the region is attributed to frontal and post frontal convective clouds. Typically during the winter season in Israel, rain only forms in clouds that reach a temperature level of around $-3\,^{\circ}\mathrm{C}$ (top height of 3–5 km). Rain clouds often develop vertically to levels colder than $-15\,^{\circ}\mathrm{C}$ (top height of 5–7 km), making cold rain the dominant precipitation process (Rosenfeld, 1986). An area of low level convergence with high updrafts over the Mediterranean Sea would be favorable for cloud and precipitation formation by supplying moisture to the mid-atmosphere and speeding up mixed phase and cold rain processes (see Sect. 1.1). Ground based radar observations near the Israeli coastline show a 1:1 to 3:1 sea to land rainfall ratio during winters (Levin et al., 2004), with the ratio peak in November, suggesting a stronger contribution of LB in the early stages of winter. Further evidence for LB effect is manifested through diurnal variation of lightning activity (Altaratz et al., 2003), showing a clear maximum of flashes number over sea (land) during midnight (afternoon). A similar trend exists for the diurnal variability of rain rates (Kutiel and Sharon, 1980), with inland precipitation peaking afternoon, and coastal precipitation peaking around midnight with a second peak around noon.

The interaction between westerly gradient winds and land breeze was studied using a 2-D non-Hydrostatic numerical simulation (Khain et al., 1993). They conclude that this interaction is the main cause for precipitation in the model. The magnitude of background gradient winds and LSTD directly affect the intensity and location of precipitation with respect to the coastline. As would be expected, stronger gradient winds shift precipitation towards inland and larger Land-Sea temperature difference shifts precipitation towards the sea. Furthermore, a convective convergence zone located *offshore*, coupled with precipitation downdrafts of cold air located slightly *onshore*, may result in positive feedback and enhancement of the land breeze circulation. This feedback was shown to be crucial in sustaining the breeze circulation (Khain and Sednev, 1996; Khain et al., 1996). The optimal values of precipitation yield over land occur when the convergence zone is located 10–20 km offshore. It is important to note that topography was excluded from the model.

In this work we perform a long term study of precipitation in the coastal region, both spatially and temporally. More than 13 yr of high resolution space-borne radar data collected by the Tropical Rain Measurement Mission (TRMM) satellite are used. Furthermore, the coastline mesoscale dynamics and roughness effects on the precipitation are separated from the orographic forcing. Section 2 discusses the methods used to retrieve and analyze the observational data. In Sect. 3 the results of the study are presented and in Sect. 4 we discuss the results in light of physical mechanisms reviewed in previous works and other dynamical theories.

2 Methods

High resolution precipitation data ($\sim 5 \times 5\,\mathrm{km}^2$ footprint) was acquired from NASA's Tropical Rainfall Measurement Mission (TRMM) database (for data see: http://mirador.gsfc.nasa.gov). TRMM satellite has been in orbit since 1997 and is equipped with both active and passive remote sensing instruments. Its main advantage compared to other precipitation measuring satellites is the first of a kind 13.8 GHz precipitation radar installed onboard, which enables NASA to obtain high resolution vertical profiles (250 m) of precipitation. TRMM covers 35° N to 35° S in a non-sun-synchronous orbit, providing spatial and temporal statistics for the tropics and sub-tropical regions.

2.1 TRMM 2A25

The TRMM product used in this work was the level 2, precipitation radar (PR) based 2A25 product (version 7), that provides vertical profile estimations of rain-rates. The product has a horizontal resolution of $\sim$5 km ($\sim$4 km before

August 2001) at nadir. The total swath is 250 km and the vertical profile ranges from the surface up to 20 km above the earth's ellipsoid, with a resolution of 250 m (i.e. total of 80 vertical levels). The 2A25 algorithm relies on a hybrid attenuation correction method which combines the surface reference technique (SRT) and Hitschfeld-Bordan method (Iguchi et al., 2000; Meneghini et al., 2000; Meneghini et al., 2004). Retrieval errors of the algorithm are mainly attributed to the uncertainty of the a prioi selected drops size distribution (DSD), incorrect physical assumptions (freezing height, hydrometeor temperatures) and non-uniform beam filling (NUBF) effects (Iguchi et al., 2009). Moreover, areas with large surface reference gradients (such as steep mountains) are subject to larger variance in the path attenuation estimation, and should therefore be dealt with caution (Meneghini and Jones, 2011). Due to the wavelength and effective signal to noise ratio of the PR (Kozu et al., 1994), 2A25 is inherently less sensitive to weak rain and drizzle ($<0.7\,\mathrm{mm\,h^{-1}}$) which are common in cases of shallow cumulus and stratiform clouds. For more on the algorithm outline and uncertainties, see papers above.

Column Integrated Hydrometeor Mass (IHM; $\mathrm{kg\,m^{-2}}$, derived from vertical profiles of rain rates) was used in this study. Integrated Hydrometeor Mass (IHM) was taken for several reasons. First, using information from all vertical levels allows more robust analysis of larger statistics compared to if only one vertical level was considered. Second, we get a measure of the total amount of liquid and solid hydrometeors throughout the vertical profile (a similar measure to the commonly used LWP variable). Finally, using integrated mass minimizes data variability in comparison to other parameters, such as surface rain rate or maximum rain rate in the column. IHM values in this work are not normalized by the number of rain days, and cannot be considered an accurate measure for accumulated rain at the surface. Nevertheless, we found that IHM and simultaneous surface rain rate are linearly correlated with $R^2 = 0.89$, and therefore can assume that IHM is proportional to rain rates at the surface.

Many validation studies have been conducted for the 2A25 product. Validation results vary on spatial and seasonal temporal scales (Nicholson et al., 2003; Wolff et al., 2005), and are regionally dependent (Franchito et al., 2009). Like all TRMM level 2 products, 2A25 is outperformed in estimating accumulated rainfall by lower resolution, rain-gauge calibrated TRMM products such as the 3B42 (Kummerow et al., 2000; Adeyewa and Nakamura, 2003; Nicholson et al., 2003). Nevertheless, 2A25 product has successfully been able to capture diurnal precipitation and climatological trends (Shin et al., 2000; Yang and Smith, 2006), and is considered to be well calibrated compared to ground validation radars (Wang and Wolff, 2009; Liao and Meneghini, 2009; Fisher and Wolff, 2010). Moreover, some of the weaknesses in performance (i.e. underestimation of rain-rates and surface clutter) over land compared to over sea previously reported (Wolff and Fisher, 2008; Iguchi et al., 2009) are expected to improve considerably as surface reference resolution increased from 1° to 0.1° and Z-R relations over land were recalibrated (changes done in the new version 7 product used in this work). In coastal regions, 2A25 is especially favorable compared to other rain products because of its high spatial resolution and relative insensitivity to land-sea surface transitions. Results based on the more commonly used passive microwave sensors raise serious doubts when used in coastal regions (McCollum and Ferraro, 2005).

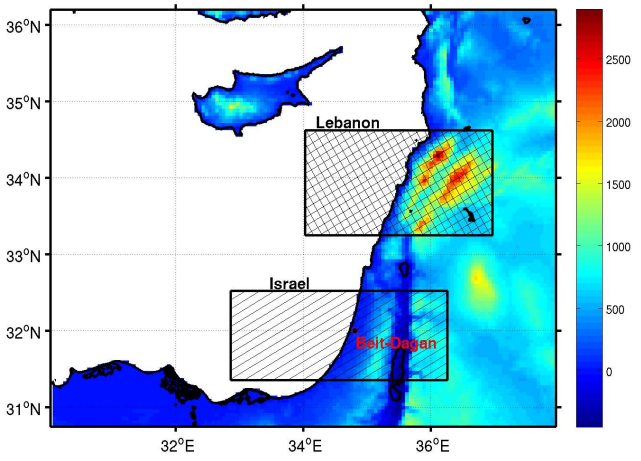

Fig. 3. Study area ROI, additional sub-regions, and Beit-Dagan meteorological station location. The color bar represents topographic height above sea-level (m). It should be noticed that both sub-regions include two successive mountain ranges nearly parallel to the coastline, but with Lebanon's mountains being higher and closer to the coast.

Considering the uncertainties of 2A25, and our main goals, we decided to focus our attention on the qualitative and not quantitative conclusions that can be derived from the rain data.

2.2 Region of interest and distance from coastlines

We focus the study on the East Mediterranean (EM), the region of interest (ROI) spans from 30° N–36° N (TRMM's northern limit) and 30° E–38° E (see Fig. 3). 2A25 data was collected for 13 winter seasons (November–March) from 1998 till 2011. The data was spatially sorted into a $5\,\mathrm{km} \times 5\,\mathrm{km}$ uniform grid that corresponds best to TRMM level 2 data. High resolution (2 min of a degree $\sim = 3.5\,\mathrm{km}$) coastline and topography data was taken from NCEP/NCAR (see: http://dss.ucar.edu/datasets/), and linearly interpolated to fit the ROI grid. Using all datasets, we sorted the TRMM data as function of distance to the nearest coastline (i.e. the normal from the coastline to each grid pixel). All results in this work are displayed with respect to distance from the nearest coastline, with positive (negative) distances corresponding to rain over land (sea). The error was taken to be $\pm 7\,\mathrm{km}$, which is the diagonal between two pixels.

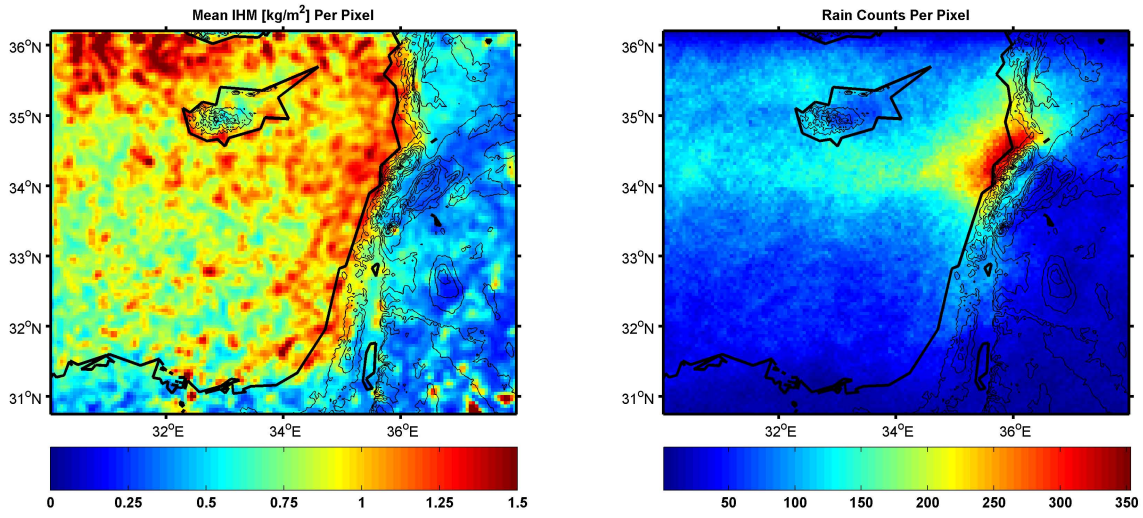

Fig. 4. Left: mean IHM (kg m^{-2}) per pixel. Right: Rain counts per pixel detected by TRMM. Data includes EM winter seasons 1998–2011. Black topography contours with vertical resolution of 300 m are added. We focus the study on the high IHM values seen near EM eastern coastlines.

Two sub-regions were defined in order to focus on the possible dynamic forcing nearby coastal areas (see Fig. 3). One named "Lebanon" and corresponds to the Lebanese region which is characterized by two extreme high mountain ridges, one of them located in close proximity to the coastline. The first ridge (referred to as Mount Lebanon ridge) peaks around 20–25 km inland, followed by successive second ridge (referred to as Anti-Lebanon ridge) located 60 km inland. Both Lebanon ridges are of comparable heights (average of ∼1.5 km), and are separated by a high elevation plateau. The second sub-region named "Israel", and corresponds to the central part of Israel. The sub-region consists of two high mountain ridges as well, although not as steep as in Lebanon and not located as close to the coastline. The first mountain ridge (referred to as Judea ridge) reaches its highest elevation (average of ∼600 m) 45–50 km inland. Judea ridge is followed by a sharp drop in elevation down to the Jordan Valley and a rapid rise afterwards to the second mountain ridge (referred to as Jordan ridge). Jordan ridge reaches its highest elevation (average of ∼700 m) 110–120 km inland. The distinct differences (i.e. ridges' height and proximity to coastlines) between both sub-regions may help us better estimate the role orographic forcing has on precipitation processes compared to other precipitation promoting dynamical effects.

2.3 Intra-seasonal and diurnal variability

From reasons discussed above (see Sect. 1.2), we divided the data analysis to two sub-seasons, one autumnal (November–December) and one wintery (January–March). Preliminary analysis of the data confirmed that there indeed is a distinct difference in IHM quantities and spatial distribution between the two sub-seasons. Moreover, we analyzed EM 850 hPa wind and 500–1000 hPa layer thickness data from NCEP reanalysis (see: http://www.esrl.noaa.gov/psd/data/gridded/) which correspond to the rain events during the study time span. The 850 hPa wind average increases during the winter season, from 5.1 m s^{-1} during November–December, to 6.8 m s^{-1} during January–March, further indicating that pressure systems in the EM are more intense during the second part of winter. The 500–1000 hPa thickness is proportional to the average virtual temperature between the two pressure levels, i.e. Hypsometric equation (Wallace and Hobbs, 2006b). The average thickness decreases from 5607 m during November–December to 5550 m during January–March, indicating that the atmosphere is cooler during the January–March sub-season.

Another type of meteorological data used in this study is the radiosonde wind and temperature data from the Beit-Dagan Israeli Meteorological Service station (Beit-Dagan is located in central Israel, approximately 10 km inland. See Fig. 3). The data was collected for rain days in Israel sub-region. The station provides two soundings per day, one at 00:00 UTC (02:00 LT) which represents the nighttime conditions, and the other at 12:00 UTC (14:00 LT) which represents the early afternoon.

3 Results

An overview of EM average IHM and total rain counts per grid pixel (icluding all 13 winter seasons) is displayed in Fig. 4. A 3 pixel × 3 pixel (15 km × 15 km) 2-D filter was applied to the IHM data to reduce statistical variance and smooth out the image. TRMM overpasses with no rain were

not included in the averaging, because we are interested in average IHM values that represent rainclouds in this region. It is important to stress that the IHM results are not normalized by the number of counts per pixel. Hence, IHM values represent the characteristic hydrometeor profile per precipitation event and not accumulated measures such as accumulated rain for the entire winter.

Despite the large variance, a band of high IHM relative to the rest of the domain can be distinguished nearby the northern and eastern coastlines of the EM. The band represents an area of enhanced precipitation formation, with vertically developed clouds and high rain rates throughout the vertical profile. Marine areas which coincide with common Cyprus low center locations (latitudes 34°–36°) also exhibit high average IHM values. Cyprus coastal area is unique. Cyprus is an island, located in the northern part of the Mediterranean sea and characterized by significant topography. As a result it exhibits special features of rain-rates around its coasts, and due to that will not be analyzed in this work. Pixels with extremely high IHM ($>1\,\mathrm{kg\,m^{-2}}$) at the south eastern part of the domain should be neglected due to poor statistics.

Due to its special orbit, TRMM overpasses latitudes 34°–35° almost twice as frequently as the rest of the domain. Thus, the orbit is the primary factor for rain counts variations in Fig. 4. Nevertheless, when considered per latitude, the number of rain counts per pixel may indicate preferred areas for rain, which are dictated by the synoptic and mesoscale features in the EM. As can be expected, TRMM detected more rain events above sea than above land. Proximity to Cyprus low center locations, to orographic barriers, and coastlines, can also be considered as factors that increase rain events. The maxima in rain counts seen near Lebanon's northern coastlines can be attributed to the combination of factors mentioned above. Additionally, given the persistent SW wind component during winter storms, the longest streamlines of moist air flow reach that same area.

We can explain the highlighted coastal band of IHM distribution in Fig. 4 by three main dynamical mechanisms: The convergence of LB and synoptic winds, frictional convergence in transition from sea to land terrain, and orographic lifting. Hence, further analysis is needed to differentiate between these mechanisms. In the next sections we shall focus on the spatial and temporal patterns of IHM in the EM subregions.

3.1 Israel

Analysis for Israel is based on 941 different rain events, where for half of the events rain was detected in more than 20 pixels and for a fifth of the events in more than 100 pixels. Figure 5 shows the daytime and nighttime histograms of low-level zonal winds in central Israel, using Bet Dagan sounding data. The average zonal wind speed between 1000 hPa (∼50 m) and 940 hPa (∼600 m) was taken as a characteristic value for the low-level boundary layer flow. The histograms roughly correspond to gaussian distributions, hence their mean values are used as representing values. During November–December the mean zonal wind speed is $-0.02\,\mathrm{m\,s^{-1}}$ (easterly wind) at night (00:00 UTC) and $2.38\,\mathrm{m\,s^{-1}}$ (westerly wind) in the afternoon (12:00 UTC). During January–March the mean wind speed is $0.90\,\mathrm{m\,s^{-1}}$ at night and $3.46\,\mathrm{m\,s^{-1}}$ in the afternoon. A consistent diurnal shift in the wind direction can be seen for both subseasons. Westerly winds are dominant during the afternoon, and display a shift to more easterly winds during the nighttime. Moreover, a similar intra-seasonal shift is seen, as easterly winds are more common in November–December compared to January–March. These observations are consistent with the basic assumption that land breezes intensify at night during the whole winter season (due to higher cooling rate of the ground compared to the sea surface) and are more pronounced during the autumnal sub-season (see Sect. 1.2). Although we don't analyze observational wind data for other locations in the EM, we can expect to see similar wind regimes in the other sub-regions as well.

As seen above, it is necessary to analyze smaller regions of well specified topography in order to try and separate between the hypothesized dynamical effects on precipitation formation. Mean IHM (Integrated Hydrometeor Mass) as a function of the distance to the coastlines for the "Israel" sub-region (see Fig. 3) is shown in Fig. 6. The IHM data was divided into liquid phase and ice phase hydrometeors and sorted into 20 bins (counts per bin appear in figure caption). The average topography profile as a function of the distance from the coast is displayed in Fig. 6 as well. Some caveats regarding the division to ice and liquid hydrometeors should be noted. The algorithm bases the division on freezing level height which is derived from climatology or bright-band height if it exists. Furthermore, all hydrometeors above the $-20\,^{\circ}\mathrm{C}$ height are considered as ice. Consequently, misclassification of mixed phase hydrometeors (such as supercooled droplets and graupel particles) is likely to occur. We therefore use the division to ice and liquid as a measure for hydrometeor height. As the freezing level is usually between 2–4 km during winter storms in Israel (based on Bet Dagan soundings data, not shown here), the division of hydrometeor mass into liquid and ice provides us extra information. Information on the characteristic vertical distribution of hydrometeors in Israel winter clouds, i.e. where most of the precipitation mass concentrated in the cloud. Additionally, we can use the ice phase hydrometeors spatial distribution as a tracer for areas likely to experience deep convective clouds with hydrometeors well above the freezing level.

The data in Fig. 6 exhibits noisy patterns, but general trends can be clearly recognized. According to our basic assumptions, we classify IHM peaks slightly offshore as convergence between synoptic winds and LB, peaks slightly onshore as FC (Frictional Convergence), and peaks nearby topographic obstacles as OF (Orographic Forcing). Results for November–December show higher IHM values over the

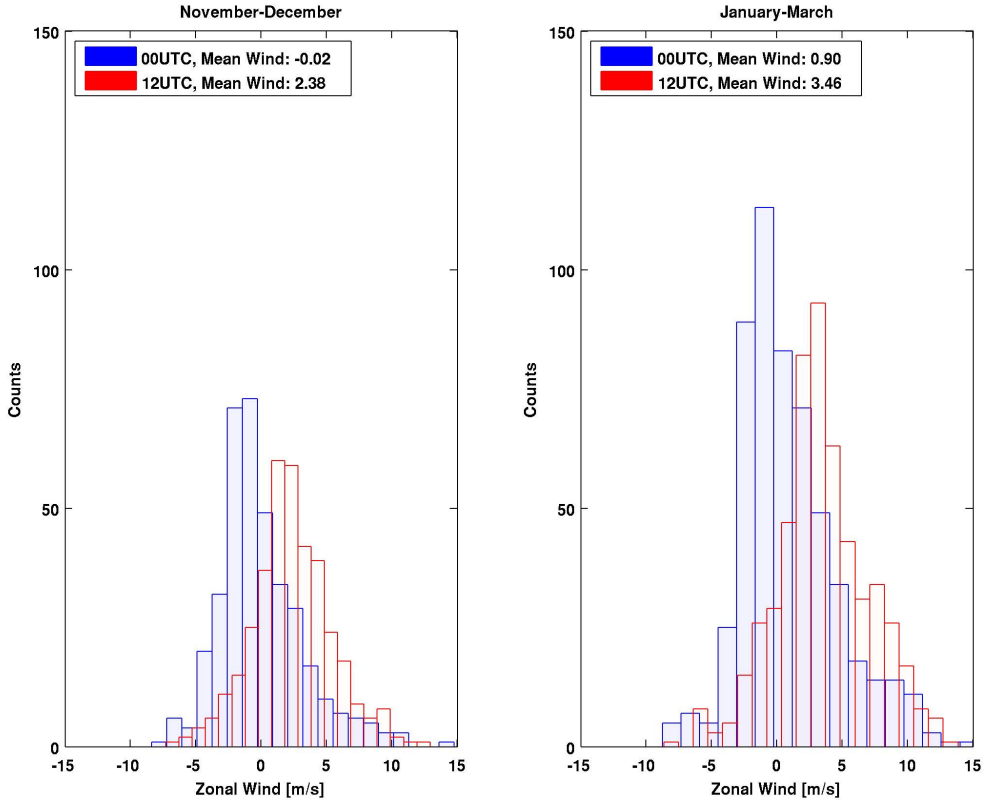

Fig. 5. Histograms of low-level zonal winds on rain days measured by Beit-Dagan (Israeli Meterological Service) radiosondes, left figure corresponds to November–December months, and right figure to January–March. Nighttime (00:00 UTC, blue color) and afternoon (12:00 UTC, red color) soundings are superimposed. The average zonal wind speed between 1000 hPa (∼50 m) and 940 hPa (∼600 m) was taken as a characteristic value for the low-level boundary layer flow.

sea than over the land, as can be expected given the warm SST in this sub-season. Values are relatively constant from -125 ± 7 km until -68 ± 7 km, where there is a sharp rise that peaks around -30 ± 7 km offshore. The IHM LB peak maximum is clearly seen offshore for both ice and liquid phases, indicating the offshore location as a preferred deep convective area. Total IHM values remain relatively high up to the coastline and decrease inland. Over the land, we can identify two localized IHM peaks (for both phases) which are likely related to orographic lifting, one at 30 ± 7 km and the other at 78 ± 7 km. The OF peaks are located around 20 km and 40 km upwind the Judea, Jordan mountain ridges' peak elevations, and seem to correspond to the location with the largest slopes (see the green curve in Fig. 6). Generally during this sub-season, the LB effect dominates offshore precipitation formation and affects a larger area than the narrow orographic effects, which dominate onshore precipitation formation peaks. We see no indication for a FC peak.

During the January–March sub-season the IHM spatial pattern changes from sea dominated to coastal dominated high values. A steady rise of liquid IHM can be seen from -75 ± 7 km towards the coast, which peaks right on the coastline (0 ± 7 km). The offshore rise can be related to LB effects, and the coastal peak is a likely a combination of LB and FC effects. However, ice IHM is constant offshore and only shows a sharp signal at the coastline which slowly decays inland, meaning that contrary to early winter, in January–March the coastal to slightly inland areas exhibit the deep convective activity signature. The repeated existence of the two OF peaks at similar (within margin of error) locations (although only seen in the liquid IHM signature) strengthens the assumption that those localized peaks are indeed orographic related.

Looking at both sub-seasons, we can see the most of the IHM can be attributed to liquid water. The average ratio of liquid IHM:ice IHM is 2.4:1 during November–December and 2.1:1 during January–March. An intra-seasonal reduction of total IHM average from 1.09 to 0.75 kg m^{-2} is observed, a decrease of ∼30 %. Lower temperatures, which imply reduced atmospheric water content, can partly explain these intra-seasonal changes as will be discussed later on.

More insight on the possible causes for the IHM spatial distributions can be obtained by sorting the IHM data according to the observed low-level zonal winds (see Fig. 5). The results are presented in Fig. 7. For each sub-season, the rain events detected by TRMM were classified here as

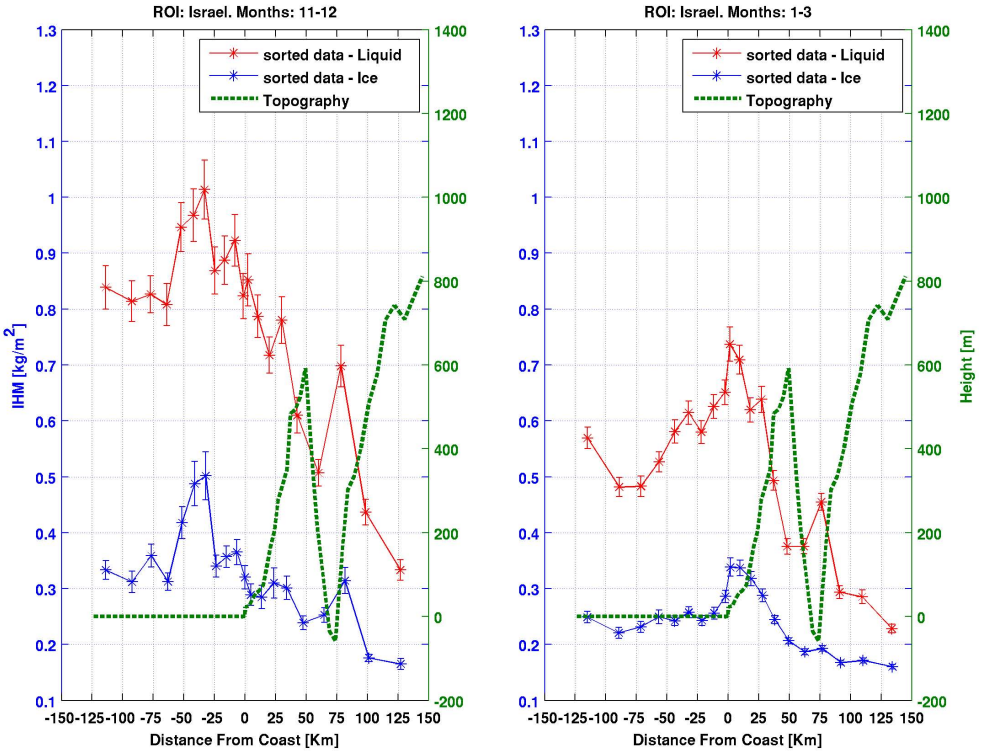

Fig. 6. Mean IHM ($\mathrm{kg\,m^{-2}}$) as a function of the distance from the nearest EM coastline, left figure corresponds to November–December months, and right figure to January–March. Positive (negative) x-axis distances correspond to rain over land (sea). The data was sorted into 20 bins according to distance from nearest coastline and divided into liquid (Red astrix curve) and ice (Blue astrix curve) phases. Error bars represent standard error of the mean. Mean topography profile (dashed green curve) is included; Judea and Jordan ridges reach their highest elevation at 46 km and 115 km, respectively. The November–December, January–March counts per bin are 1184, 2550 for liquid IHM and 1002, 2433 for ice IHM, respectively.

day (08:00 LT to 20:00 LT) or night (20:00 LT to 08:00 LT) events. The median wind velocity was then calculated for day and night separately using the Bet Dagan sounding data. Half of the total soundings that represent days and nights with easterly and weak westerly winds were classified as WW (Weak Wind) events, and the other half that represent days and nights with medium to strong westerly winds as SW (Strong Wind) events.

For November–December months, the separation to WW and SW events exposes two regimes. For WW (Weak Wind) events, we see a clear LB peak for both liquid and ice phases. A sharp drop in ice IHM is seen in transition from sea to land, indicating a preference for deep convection offshore. The LB peak is widespread, covers the distances from -75 ± 7 km to the coastline, and reaches its maximum value around -35 ± 7 km. Localized OF peaks in liquid IHM are located within the margin of error of those seen in Fig. 6, and are much weaker than the LB peak. Ice IHM values increase over the mountains and reach a local maximum around 75 ± 7 km.

For SW (Strong Wind) events, no distinct offshore peak can be recognized. Over the sea, liquid and ice IHM values are high and relatively constant, and drop gradually over land, where small IHM OF peaks (liquid and ice) can be seen at 23 ± 7 km (attributed to the Judea ridge) and at 78 ± 7 km (attributed to the Jordan ridge). Interestingly, ice IHM shows a strong signature at around -40 ± 7 km for SW events, similarly to WW events. No matter what wind regime exists, the -50 ± 7 to -20 ± 7 km offshore location is a preferred location for deep convection during the first sub-season. These results support our hypothesis that during WW events convergence zones exist offshore, and are not as prominent during SW events. There are OF signatures at similar locations during all events, implying that wind-topography interactions have a similar effect for both wind regimes. However, for WW events the deep convective signature is larger over Jordan ridge and for SW events the deep convective signature is larger over Judea ridge.

The IHM distribution differences between WW and SW events during January–March in Fig. 7 are more subtle. For both WW and SW events, liquid IHM values rise from deep sea towards the land, and peak nearby the coast. The peak for WW events is located around 20 ± 7 km, favoring OF effect, and the peak for SW events is located at 0 ± 7 km (coastline), favoring FC effect. An indication for a LB peak in

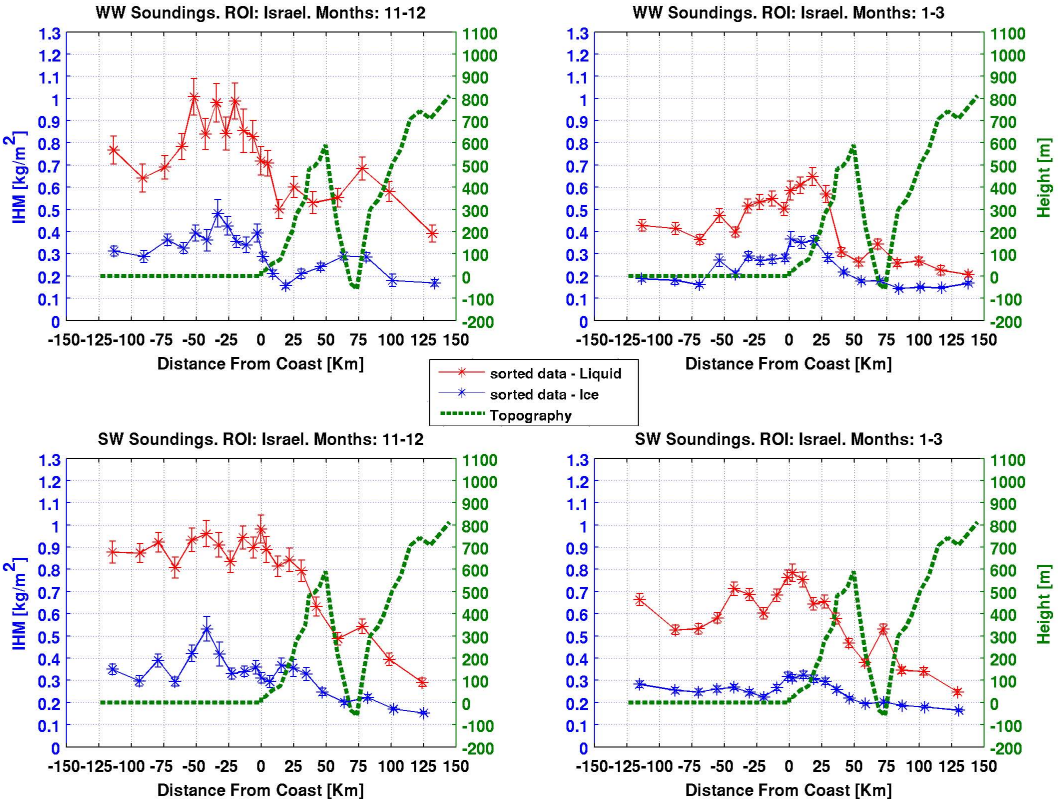

Fig. 7. Same as Fig. 6, but with data separated to WW (upper two figures) and SW events (lower two figures). Weak Wind (WW) events correspond to soundings with easterly and weak westerly low-level winds. Strong Wind (SW) events correspond to soundings with moderate to strong westerly low-level winds. For WW events, the November–December, January–March counts per bin are 362, 663 for liquid IHM and 319, 638 for ice IHM, respectively. For SW events, the November–December, January–March counts per bin are 813, 1314 for liquid IHM and 683, 1239 for ice IHM, respectively.

liquid IHM is only seen during SW events at -40 ± 7 km. However, the ice IHM trends favor a LB effect during the WW events, where there is a plateau of higher ice IHM values from -70 ± 7 km to 25 ± 7 km, which may correspond to the total possible range of LB effect. During SW events ice IHM remains relatively flat and rises after a local minima at -22 ± 7 km, reaching highest values from the coastline to 20 ± 7 km inland, gradually decreasing afterwards. Once more, orographic (Judea and Jordan) IHM peaks can be seen at the same spatial locations for both WW and SW events (mostly in liquid IHM), with minor differences between them.

Additional wind analysis was performed (results not displayed here) using SeaWinds aboard QuikSCAT (Quick Scatterometer) mission (Graf et al., 1998). QuikSCAT obtains near surface wind vectors with a spatial resolution of 25 km × 25 km and passes over the same terrain twice every day, at 06:00 (early morning) and 18:00 (late afternoon) LST. The instrument is limited to marine surfaces reaching to about 25 km offshore the coastlines. Using the wind vector data, we calculated wind divergence for the EM region during rain events and reached two main conclusions: (i) offshore coastal areas (excluding Cyprus island) up to 100 km offshore experience near surface negative (positive) wind divergence during the early morning (late afternoon) hours. (ii) Far offshore areas show no wind divergence in the morning and slight positive divergence in the afternoon. These conclusions are valid for both sub-seasons, and serve as another indication that mesoscale convergence occurs nearby coastlines during the night and early morning when LBs more frequently occur.

As previously discussed, if LB interaction with gradient winds, frictional convergence and orographic lifting are considered to be the physical mechanisms behind the highlighted IHM band, we would expect to see a diurnal pattern. Nighttime experiences the largest SST-Land temperature difference, so we would expect to see the strongest and furthest offshore IHM signal during the night. Radiative surface heating (though limited due to cloud shading) of land and mountain slopes should result in an opposite effect, with a maximum IHM signal over land during the day. Frictional convergence effects are not likely to show any distinct diurnal pattern. We stress the point that diurnal IHM variations in this work do not necessarily reflect a typical diurnal variation per winter

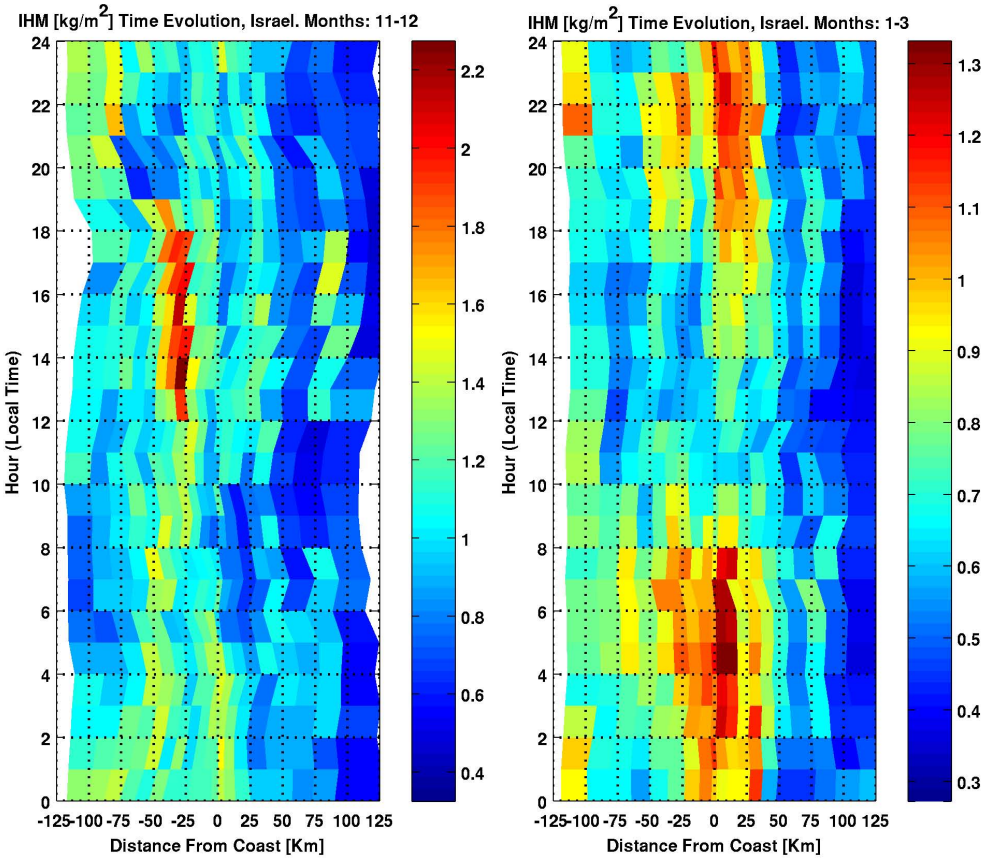

Fig. 8. Integrated Hydrometeor Mass (liquid+ice) time evolution with respect to coastline for November–December (left figure) and January–March (right figure), in the "Israel" sub-region. Color bar scale represents IHM ($kg\,m^{-2}$); notice that color bars are scaled differently for each sub-season in order to enhance the diurnal variance. Data was sorted as a function of distance from nearest coastline and local time (into 20 bins). Y axis numbers are the center local time of the ± 3 h averaging time span, running from 00:00 (midnight) to 24:00. To interpret the Y axis: 0–5 should be considered nighttime hours, 6–11 morning hours, 12–17 daytime hours and 18–23 evening hours. Pixel width reflects the density of counts, narrow pixels being denser. The November–December, January–March mean counts per bin are 302, 647, respectively.

storm, but rather the diurnal preferences for precipitation in a climatological view. The satellite data used gives us only fragments of storms and instantaneous snapshots, therefore the existence of two different peaks at the same hour can be due to the combination of several different events or just one event with multiple effects taking place.

To support the idea that diurnal variations are due to mesoscale dynamics and not synoptic scale forcing, we checked the diurnal variation of IHM far away from coastlines (more than 150 km offshore). Eastern Mediterranean winter storms do (on average) display a pseudo-sinusoidal IHM signal, with a maximum between 08:00–11:00, and minimum between 20:00–24:00. However, the amplitude is less than $0.1\,kg\,m^{-2}$, at least three times smaller than the IHM diurnal cycle amplitudes near the coastlines. The time evolution of the IHM distribution with respect to the coastline in Israel is displayed in Fig. 8. To reduce the noise, we used a moving ± 3 h span average, e.g. the data from 6 (Local Time) is an average of the data collected between 03:00 and 09:00 (see Fig. 8 caption for more details on diurnal analysis).

Both winter sub-seasons show an IHM diurnal cycle that partly fits the land-sea temperature difference diurnal evolution. During November–December, the peak of the IHM distribution propagates offshore as the night progresses, reaching a maximum extent around $08{:}00 \pm 3$ h. The offshore peak stays intact and intensifies during daytime hours (12:00–$18{:}00 \pm 3$ h), a fact that does not fit with our explanation that is based on the land-sea temperature difference (LSTD) diurnal evolution. The Judea and Jordan orographic peaks (at $\sim$30 km and $\sim$80 km inland) show maximum values during the afternoon ($12{:}00$–$18{:}00 \pm 3$ h) as well.

During January–March, the IHM distribution shows a strong diurnal pattern which follows the land-sea temperature difference. The IHM peak is centered near the coastline, it intensifies and widens offshore during the evening and night and reaches an offshore maximum extent around $06{:}00$–$07{:}00 \pm 3$ h, with sunrise. During the daytime the

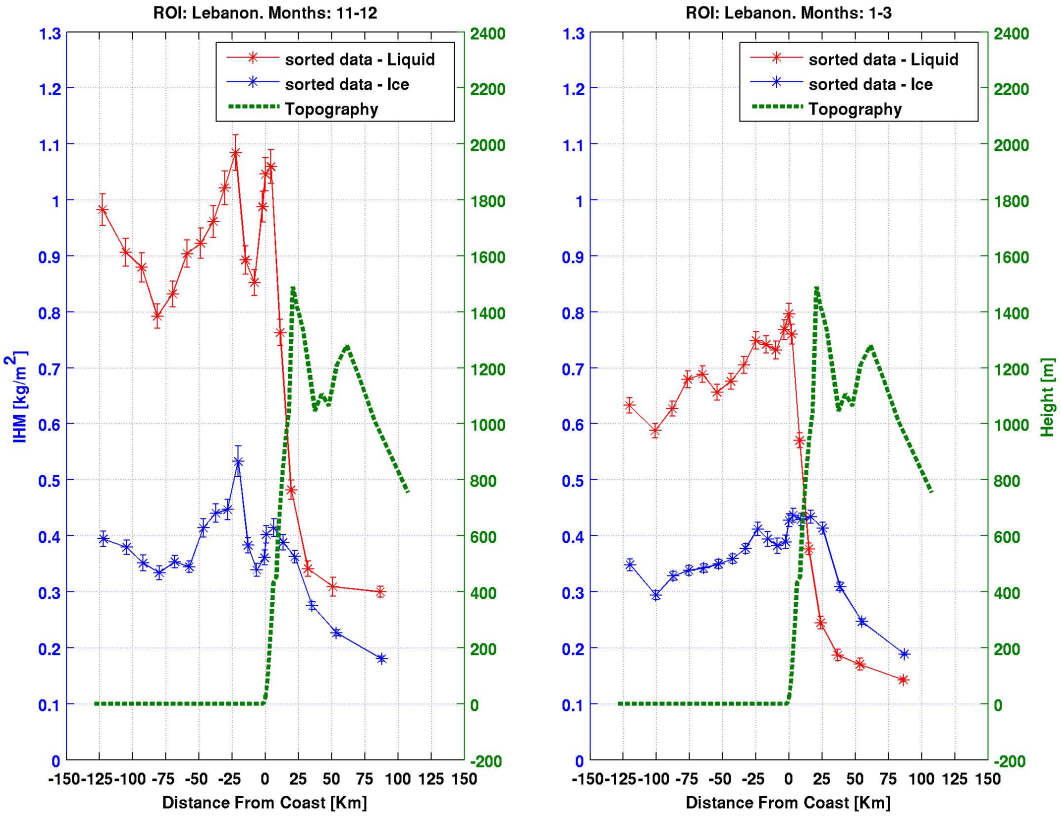

Fig. 9. Same as Fig. 6, but for "Lebanon" sub-region. The two ridges reach their highest elevations at 21 km and 60 km inland. The November–December, January–March counts per bin are 3743, 6754 for liquid IHM and 3507, 6719 for ice IHM, respectively.

LB peak clearly decreases while onshore IHM values dominate the distribution. The orographic peaks no longer display daytime maxima. Judea peak seems to intensify during the evening and night (18:00–08:00 ± 3 h), and the Jordan peak reaches its maximum values during the morning (06:00 ± 3 h) and evening (18:00 ± 3 h) hours. A pronounced feature of both sub-seasons is the IHM local minima located at the rain shadow of the Judea ridge.

3.2 Lebanon

The "Lebanon" sub-region (see Fig. 3) spatial distribution of liquid and ice IHM is shown in Fig. 9. Analysis for Lebanon is based on 1545 different rain events, where for half of the events rain was detected in more than 20 pixels and for a third of the events in more than 100 pixels. Two clear IHM peaks are seen during November–December. The high Mount Lebanon ridge dominates the coastal plain and serves as a barrier for the flow, therefore we classify the peaks as a combined OF+FC peak, and a LB induced peak. We tag the peak at -23 ± 7 km as related to LB effect, and the other at the coastline (about 20 km upwind the ridge's max elevation) as related to OF and FC effect. The LB peak is more widespread, and influences IHM values up to -80 ± 7 km offshore. Moreover, similar to Israel, the LB peak ice IHM signal is stronger than the orographic one, indicating a more deep convective nature for precipitation offshore. The high liquid IHM values between -125 ± 7 km and -80 ± 7 km might be due to the proximity to the Cyprus low centers or Cyprus island coastline effects (see Fig. 4). Total IHM values decrease exponentially with distance downwind the Mount Lebanon ridge, what seems to be a strong rain-shadow effect.

The offshore LB peak nearly disappears during January–March. We see a steady rise of liquid and ice IHM from deep sea towards the coast, with highest values at the coastline. The OF+FC peak dominates this sub-season, although traces of a LB peak can be seen at -25 ± 7 km. Unlike the previous figures, we can see that ice IHM values are higher than liquid IHM values inland Lebanon. Colder temperatures and higher topography can explain this. Focusing on the area upwind the Mount Lebanon ridge, the average ratio of liquid IHM:ice IHM is 2.3:1 during November–December and 1.7:1 during January–March. Inland Lebanon (after the first mountain ridge) ice and liquid IHM are comparable. An intra-seasonal reduction of total IHM average from 1.29 to 1.04 kg m^{-2} is observed, a decrease of ∼19 %. Diurnal patterns of IHM for "Lebanon" sub-region are shown in Fig. 10. Considering the November–December sub-season, the separation to

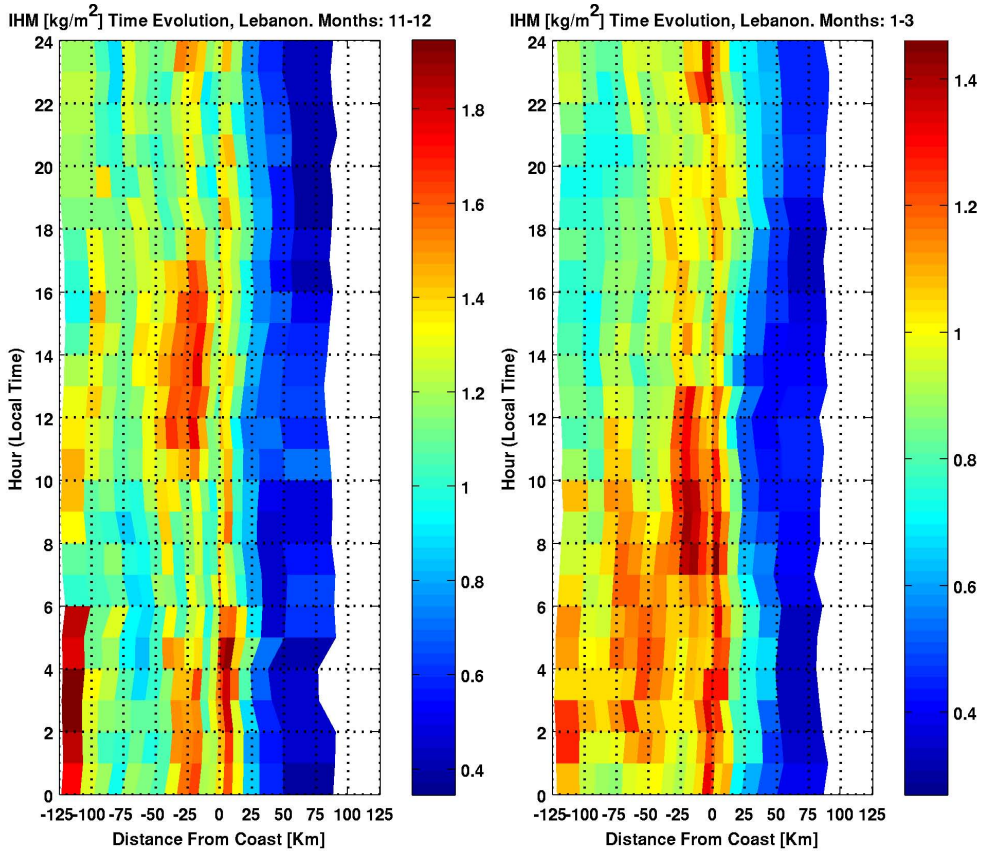

Fig. 10. Same as Fig. 8, but for "Lebanon" sub-region. The November–December, January–March mean counts per bin are 957, 1740, respectively.

two peaks is clearly seen throughout the diurnal cycle. The offshore LB peak displays two modes of high IHM values: (i) during nighttime hours (23:00–05:00 $\pm$ 3 h) (ii) during daytime hours (11:00–17:00 $\pm$ 3 h), exhibiting similar behavior to the Israel sub-region offshore peak during November–December. Moreover, the distribution spreads offshore to its largest distance during daytime and not nighttime as expected. The combined FC and OF peak IHM values remain more stable throughout the diurnal cycle, showing maximum values during the nighttime (00:00–06:00 $\pm$ 3 h). The -120 km offshore peak which is attributed to Cyprus sub-region generally follows the LB peak diurnal cycle.

January–March shows different behavior than November–December. The separation to LB and orographic peaks is less obvious, and can only be distinguished during the morning hours. The LB and OF+FC peaks reach their minimum magnitude during the late afternoon and early evening. Both peaks (LB and OF+FC) intensify during the nighttime and morning hours (00:00–12:00 $\pm$ 3 h). High IHM values show the same offshore spreading effect as previously seen in Israel sub-region. During the nighttime (00:00–06:00 $\pm$ 3 h), the LB peak spreads out and peaks and covers the areas between -75 ± 7 km and -25 ± 7 km from the coastline. Daytime hours experience a LB peak transition to areas between -30 ± 7 km and -5 ± 7 km. This sub-season shows good agreement between offshore IHM peak locations and LSTD diurnal changes.

4 Summary and discussion

Precipitation data in this work is represented by Mean Integrated Hydrometeor Mass (IHM; kg m^{-2}), which serves as a measure of the average instantaneous precipitation amounts throughout the cloud vertical column. The use of IHM is conceptually different from most precipitation studies, which focus on accumulated ground rainfall (mm). The differences between IHM values (that represent the characteristic precipitation profile) and accumulated rainfall can be demonstrated by their intra-seasonal evolution. Taking the coastal cities of Tel-Aviv (Israel), Larnaka (Cyprus), and Lattakia (Syria) as representing examples, accumulated rainfall increases from 205, 128, 255 mm during November–December to 276, 165, 351 mm during January–March (data taken from the World Meteorological Organization (WMO) website, http://worldweather.wmo.int), an increase of 34 %,

28 %, and 37 %, respectively. This is in contrary to IHM values in Israel (Lebanon), which decrease 30 % (19 %). To try and explain this decrease, we collected Precipitable Water (The total atmospheric water vapor contained in a vertical column of unit cross-sectional area; $\mathrm{kg\,m^{-2}}$) data for the corresponding rain dates from NOAA-NCEP Global Data Assimilation System (GDAS), for details see: (Parrish and Derber, 1992; Saha et al., 2010). Average Precipitable Water values for the Israel region decrease ∼22 % (from $18.60\,\mathrm{kg\,m^{-2}}$ to $14.52\,\mathrm{kg\,m^{-2}}$), and Lebanon region values decrease ∼20 % ($18.52\,\mathrm{kg\,m^{-2}}$ to $14.67\,\mathrm{kg\,m^{-2}}$). Therefore, a significant portion of the intra-seasonal decrease in average IHM values can be attributed to the decrease in atmospheric water content.

The results in this work support the idea that low level convergence of LB and synoptic winds near the sea-land interface have a substantial effect on precipitation formation in the region. Frictional convergence near the coast and high topographic ridges (Mount Lebanon, Judea and Jordan) in the region also affect IHM distributions. The existence of the narrow orographic peaks at approximately the same locations during the entire winter and for all wind regimes serves as conformation that those peaks are due to a stationary effect. For both Israel and Lebanon sub-regions, the orographic IHM peaks are located $20–40 \pm 7$ km upwind the mountain ridges' highest elevation and correspond to the largest elevation gradients, and therefore to the largest orographic forced vertical velocities (see Sect. 1.1). There was no notable effect to the Anti-Lebanon ridge (located in Lebanon sub-region, 60 km from the coast). This may be due to depletion of much of the water content (rain shadow effect) after passing the first ridge, the smaller height gradient between both ridges, and underestimation of rain-rates which can occur over certain land areas (see Sect. 2.1).

Integrated hydrometeor Mass distributions change considerably during the winter in both sub-regions (Israel and Lebanon), as can be summarized to three main points: (i) during November–December, high offshore liquid and ice IHM values dominate the distributions, with a peak representing deep convective area at -40 ± 7 km to -20 ± 7 km and a following decrease towards the coastlines. (ii) During January–March, the main deep convective area is located at the coastline, although IHM values do increase from at least -75 ± 7 km offshore. (iii) In total, LB effects are larger and more widespread than OF and FC. The results are consistent with the assumption that LB effects are prominent during early winter (large LSTD), and frictional effects are prominent during late winter (stronger winds result in larger drag force). Even though the separation of peaks to LB and FC is artificial and only qualitatively deduced, it is supported by both the addition of the sharp ice IHM signatures and a futher division of rain dates to WW and SW events (see Sect. 3.1). Land Breeze tagged peaks are more prominent during days with weak westerly and easterly winds, especially during November–December. Frictional convergence tagged peaks are clearly seen on days with strong westerly winds, especially during January–March. Nevertheless, the possibilty that FC tagged peaks may represent the formation of LB fronts nearby the coastlines or slightly onshore should be considered.

The diurnal cycles of IHM distributions are similar for Israel and Lebanon sub-regions. During the whole winter season in Israel (with the exception of the afternoon hours in November–December), the average diurnal variation can be described as a see-saw pattern. Evening to morning hours exhibit a preference for high offshore IHM values, while late morning to evening hours exhibit a preference for high coastal and inland IHM values. The pattern fits the diurnal wind evolution seen in Fig. 5 of strong LB at night and weak LB during the day and the effects of inland solar heating during the day that can de-stabilize the atmospheric profile over the land (especially over mountains during November–December). It is apparent however, that the offshore LB peak during November–December is highly affected from the intense afternoon offshore peak centered near -30 ± 7 km (see Fig. 8), a fact which opposes our current proposed theory. The peak is present in Israel's SW events ice IHM distribution as well. To our knowledge, the afternoon peak has not been previously reported. Lebanon sub-region diurnal cycle (November–December, see Fig. 10) combined with year-by-year analysis further confirm the credibility of the diurnal pattern. Preliminary analysis of synoptic factors reveals no consistent reasons to why the afternoon peak exists. Therefore, a following work is planned to look into this diurnal feature.

Excluding the November–December afternoon offshore peak discussed above, Lebanon sub-region IHM peaks intensify during the nighttime in November–December and during the late night and morning hours in January–March. The diurnal cycles for both sub-seasons could be partially explained by LB effect; however, the cycle is fundamentally different than the cycle in Israel in two ways: (i) Mount Lebanon orographic peak stays nearly constant in intensity and location throughout the cycle. (ii) Lebanon region exhibits a strong coupling between the offshore (LB) and onshore (orographic and FC) peaks. The main differences between Israel and Lebanon sub-regions are the location and magnitude of their topographic obstacles, combined with Lebanon's closer position to the Cyprus low vortices centers. Hence, it is likely that Lebanon's IHM diurnal pattern is dominated by interaction of synoptic winds with topography.

The results of the spatial and temporal analysis are to the most consistent with higher SST-Land temperature differences during the first part of the winter, increasing LB and "pushing" the main convergence zone further offshore while the orographic influence is rather local. During the second part of winter, deeper vortices that produce stronger synoptic winds combine with weaker LB. Consequently, the convergence zone is displaced towards the land and clouds that form over the sea are advected more efficiently inland.

Additionally, the stronger winds increase frictional drag and possible interactions with topographic obstacles, further favoring precipitation formation over land.

Given the more common westerly winds, we would expect to see an inland shift of the surface rain rate distribution compared to the IHM distribution even though both are highly correlated. With the use of the surface rain rate parameter from the 2A25 product, we repeated the analysis as done for IHM and saw no consistent shift of the peak locations towards the land or sea. Moreover, by considering low end values of TRMM detectable rain rates ($\sim$1 mm h^{-1}) that can be shown to correspond to a minimal drop size of $\sim$0.7 mm (Feingold and Levin, 1986) and a terminal fall speed of $\sim$5 m s^{-1} (Wobus et al., 1971), combined with high end values for the precipitation profile center of gravity (2.5 km) and horizontal wind speed (10 m s^{-1}), we obtain a horizontal distance shift of 5 km, exactly TRMM PR's footprint. Hence, even if an inland shift exists, the resolution of our dataset is too coarse to detect it.

In this work we focused on convective precipitation processes as affected by dynamical effects of sea-land thermal differences, surface friction and topographic obstacles. We have also shown the benefits of using TRMM in high resolution mesoscale studies. Other factors not discussed here such as surface fluxes, land cover and aerosols can also influence the IHM distribution in the EM region and require further study. A numerical simulation of aerosol effect on rain delay in Israel indicates that high aerosol loadings in rainclouds may successfully shift rainfall from sea to land (Noppel et al., 2010). Hence, in light of the offshore and coastal preference for precipitation formation found in our work, aerosol seeding (with intent to delay rain) of coastal rain clouds may have promising implications on the region's water supply. Finally, we plan to investigate if similar IHM distributions exist in other mid-latitude coastal areas around the globe.

Acknowledgements. This research was supported in part by the Israel Science Foundation (grant 1172/10) and by the Minerva Foundation (grant 780048). TRMM data provided by NASA's Goddard Earth Sciences Data and Information Services Center (GES DISC). NCEP reanalysis data and images provided by the NOAA/OAR/ESRL PSD, Boulder, Colorado, USA, from their Web site at http://www.esrl.noaa.gov/psd/. GDAS data provided by NOAA/NCEP (MODIS Ancillary Data), from their Web site at http://ladsweb.nascom.nasa.gov/.

Edited by: G. Feingold

References

Adeyewa, Z. D. and Nakamura, K.: Validation of TRMM radar rainfall data over major climatic regions in Africa, J. Appl. Meteorol., 42, 331–347, 2003.

Alpert, P., Neeman, B. U., and Shay-El, Y.: Climatological analysis of Mediterranean cyclone using ECMWF data, Tellus, Series A Dyn. Meteorol. Ocean., 42A, 65–77, 1990a.

Alpert, P., Neeman, B. U., and Shayel, Y.: Intermonthly Variability of Cyclone Track in the Mediterranean, J. Climate, 3, 1474–1478, 1990b.

Altaratz, O., Levin, Z., Yair, Y., and Ziv, B.: Lightning activity over land and sea on the eastern coast of the Mediterranean, Mon. Weather Rev., 131, 2060–2070, 2003.

Byers, H. R.: Identification of ice nuclei in the atmosphere, International Conference on Cloud Physics Tokyo, 126–130, 1965.

Feingold, G. and Levin, Z.: The Lognormal Fit to Raindrop Spectra from Frontal Convective Clouds in Israel, J. Climate Appl. Meteorol., 25, 1346–1363, doi:10.1175/1520-0450(1986)025<1346:TLFTRS>2.0.CO;2, 1986.

Fisher, B. and Wolff, D. B.: Satellite Sampling and Retrieval Errors in Regional Monthly Rain Estimates from TMI, AMSR-E, SSM/I, AMSU-B, and the TRMM PR, J. Appl. Meteorol. Climatol., 50, 994–1023, doi:10.1175/2010jamc2487.1, 2010.

Fisher, E. L.: An Observational Study of the Sea Breeze, J. Meteorol., 17, 645–660, 1960.

Fisher, E. L.: A Theoretical Study of the Sea Breeze, J. Meteorol., 18, 216–233, 1961.

Franchito, S. H., Rao, V. B., Vasques, A. C., Santo, C. M. E., and Conforte, J. C.: Validation of TRMM precipitation radar monthly rainfall estimates over Brazil, J. Geophys. Res.-Atmos., 114, D02105 doi:10.1029/2007jd009580, 2009.

Fukuta, N.: Water supersaturation in convective clouds, Atmos. Res., 30, 105–126, doi:10.1016/0169-8095(93)90043-n, 1993.

Goldreich, Y.: The Climate of Israel: Observation, Research and Application, Kluwer Academic/Plenum Publishers, 2003.

Goldreich, Y., Mozes, H., and Rosenfeld, D.: Radar analysis of cloud systems and their rainfall yield, in Israel, Israel J. Earth Sci., 53, 63–76, 2004.

Goldreich, Y., Mozes, H., and Rosenfeld, D.: Analysis of rainy cloud systems by radar and satellite images in inter-monthly variations, Merhavim, 385–396, 2006 (in Hebrew, Abstr).

Graf, J. E., Wu-yang, T., and Jones, L.: Overview of QuikSCAT mission-a quick deployment of a high resolution, wide swath scanning scatterometer for ocean wind measurement, Southeastcon '98, Proceedings. IEEE, 314–317, 1998.

Hindman, E. E. and Johnson, D. B.: Numerical Simulation of Ice Particle Growth in a Cloud of Supercooled Water Droplets, J. Atmos. Sci., 29, 1313–1321, doi:10.1175/1520-0469(1972)029<1313:NSOIPG>2.0.CO;2, 1972.

Houghton, H. G.: A Preliminary Quantitative Analysis of Precipitation Mechanisms, J. Meteorol., 7, 363–369, 1950.

Houghton, H. G.: On Precipitation Mechanisms and their Artificial Modification, J. Appl. Meteorol., 7, 851–859, doi:10.1175/1520-0450(1968)007<0851:OPMATA>2.0.CO;2, 1968.

Houze Jr., R. A.: Orographic Clouds, in: Cloud Dynamics, Academic Press, Inc., 502–538, 1993.

Iguchi, T., Kozu, T., Meneghini, R., Awaka, J., and Okamoto, K.: Rain-profiling algorithm for the TRMM precipitation radar, J. Appl. Meteorol., 39, 2038–2052, 2000.

Iguchi, T., Kozu, T., Kwiatkowski, J., Meneghini, R., Awaka, J., and Okamoto, K.: Uncertainties in the Rain Profiling Algorithm for the TRMM Precipitation Radar, J. Meteorol. Soc. Jpn., 87, 1–30, doi:10.2151/jmsj.87A.1, 2009.

Khain, A. P. and Sednev, I.: Simulation of precipitation formation in the Eastern Mediterranean coastal zone using a spectral microphysics cloud ensemble model, Atmos. Res., 43, 77–110, 1996.

Khain, A. P., Rosenveld, D., and Sednev, I.: Coastal effects in the Eastern Mediterranean as seen from experiments using a cloud ensemble model with detailed description of warm and ice microphysical processes, Atmos. Res.-Atmos. Res., 30, 295–319, 1993.

Khain, A. P., Sednev, I., and Khvorostyanov, V.: Simulation of coastal circulation in the Eastern Mediterranean using a spectral microphysics cloud ensemble model, J. Climate, 9, 3298–3316, 1996.

Kimball, S. K.: Structure and Evolution of Rainfall in Numerically Simulated Landfalling Hurricanes, Mon. Weather Rev., 136, 3822–3847, doi:10.1175/2008mwr2304.1, 2008.

Kozu, T., Kawanishi, T., Oshimura, K., Satake, M., and Kumagai, H.: TRMM precipitation radar: calibration and data collection strategies, Geoscience and Remote Sensing Symposium, 1994. IGARSS '94, Surface and Atmospheric Remote Sensing: Technologies, Data Analysis and Interpretation., International, 2214, 2215–2217, 1994.

Kummerow, C., Simpson, J., Thiele, O., Barnes, W., Chang, A. T. C., Stocker, E., Adler, R. F., Hou, A., Kakar, R., Wentz, F., Ashcroft, P., Kozu, T., Hong, Y., Okamoto, K., Iguchi, T., Kuroiwa, H., Im, E., Haddad, Z., Huffman, G., Ferrier, B., Olson, W. S., Zipser, E., Smith, E. A., Wilheit, T. T., North, G., Krishnamurti, T., and Nakamura, K.: The status of the Tropical Rainfall Measuring Mission (TRMM) after two years in orbit, J. Appl. Meteorol., 39, 1965–1982, 2000.

Kutiel, H. and Sharon, D.: Diurnal-Variation of Rainfall in Israel, Archiv Für Meteorologie Geophysik und Bioklimatologie Serie a-Meteorologie Und Geophysik, 29, 387–395, 1980.

Leighton, H. G. and Rogers, R. R.: Droplet Growth by Condensation and Coalescence in a Strong Updraft, J. Atmos. Sci., 31, 271–279, doi:10.1175/1520-0469(1974)031<0271:DGBCAC>2.0.CO;2, 1974.

Levin, Z. and Cotton, W. R.: Aerosol Pollution Impact on Precipitation: A Scientific Review, Springer, 2009.

Levin, Z., Breitgang, J., and Shtivelman, D.: Precipitation over the sea in the coastal area of Israel: a possible new source of water, 14th International Conference on Clouds and Precipitation, 2004, 1228–1231,

Levy, I., Dayan, U., and Mahrer, Y.: A five-year study of coastal recirculation and its effect on air pollutants over the East Mediterranean region, J. Geophys. Res., 113, D16121, doi:10.1029/2007jd009529, 2008.

Liao, L. and Meneghini, R.: Validation of TRMM precipitation radar through comparison of its multiyear measurements with ground-based radar, J. Appl. Meteorol. Climatol., 48, 804-817817, doi:10.1175/2008jamc1974.1, 2009.

Lu, J., Vecchi, G. A., and Reichler, T.: Expansion of the Hadley cell under global warming, Geophys. Res. Lett., 34, L06805, doi:10.1029/2006gl028443, 2007.

Ludlam, F. H.: The production of showers by the growth of ice particles, Quart. J. Roy. Meteorol. Soc., 78, 543–553, doi:10.1002/qj.49707833805, 1952.

Malda, D., Vilà-Guerau de Arellano, J., van den Berg, W. D., and Zuurendonk, I. W.: The role of atmospheric boundary layer-surface interactions on the development of coastal fronts, Ann. Geophys., 25, 341–360, doi:10.5194/angeo-25-341-2007, 2007.

McCollum, J. R. and Ferraro, R. R.: Microwave Rainfall Estimation over Coasts, J. Atmos. Ocean. Technol., 22, 497–512, doi:10.1175/jtech1732.1, 2005.

Meneghini, R. and Jones, J. A.: Standard Deviation of Spatially Averaged Surface Cross Section Data From the TRMM Precipitation Radar, Geosci. Remote Sens. Lett., IEEE, 8, 293–297, 2011.

Meneghini, R., Iguchi, T., Kozu, T., Liao, L., Okamoto, K. i., Jones, J. A., and Kwiatkowski, J.: Use of the Surface Reference Technique for Path Attenuation Estimates from the TRMM Precipitation Radar, J. Appl. Meteorol., 39, 2053–2070, doi:10.1175/1520-0450(2001)040<2053:uotsrt>2.0.co;2, 2000.

Meneghini, R., Jones, J. A., Iguchi, T., Okamoto, K., and Kwiatkowski, J.: A Hybrid Surface Reference Technique and Its Application to the TRMM Precipitation Radar, J. Atmos. Ocean. Technol., 21, 1645–1658, doi:10.1175/jtech1664.1, 2004.

Meyer, J. H.: Radar Observations of Land Breeze Fronts, J. Appl. Meteorol., 10, 1224–1232, doi:10.1175/1520-0450(1971)010<1224:ROOLBF>2.0.CO;2, 1971.

Mordy, W.: Computations of the Growth by Condensation of a Population of Cloud Droplets, Tellus, 11, 16–44, 1959.

Nelson, L. D.: A Numerical Study on the Initiation of Warm Rain, J. Atmos. Sci., 28, 752–762, 1971.

Neumann, J.: Land Breezes and Nocturnal Thunderstorms, J. Meteorol., 8, 60–67, 1951.

Nicholson, S. E., Some, B., McCollum, J., Nelkin, E., Klotter, D., Berte, Y., Diallo, B. M., Gaye, I., Kpabeba, G., Ndiaye, O., Noukpozounkou, J. N., Tanu, M. M., Thiam, A., Toure, A. A., and Traore, A. K.: Validation of TRMM and other rainfall estimates with a high-density gauge dataset for West Africa, Part II: Validation of TRMM rainfall products, J. Appl. Meteorol., 42, 1355–1368, 2003.

Noppel, H., Pokrovsky, A., Lynn, B., Khain, A. P., and Beheng, K. D.: A spatial shift of precipitation from the sea to the land caused by introducing submicron soluble aerosols: Numerical modeling, J. Geophys. Res., 115, D18212, doi:10.1029/2009jd012645, 2010.

Parrish, D. F. and Derber, J. C.: The National Meteorological Center's Spectral Statistical-Interpolation Analysis System, Mon. Weather Rev., 120, 1747–1763, 1992.

Pathirana, A., Herath, S., and Yamada, T.: Simulating orographic rainfall with a limited-area, non-hydrostatic atmospheric model under idealized forcing, Atmos. Chem. Phys., 5, 215–226, doi:10.5194/acp-5-215-2005, 2005.

Purdom, J. F. W.: Some Uses of High-Resolution GOES Imagery in Mesoscale Forecasting of Convection and its Behavior, Mon. Weather Rev., 104, 1474–1483, 1976.

Qian, J.-H.: Why Precipitation Is Mostly Concentrated over Islands in the Maritime Continent, J. Atmos. Sci., 65, 1428–1441, doi:10.1175/2007jas2422.1, 2008.

Reinking, R. F.: Formation of Graupel, J. Appl. Meteorol., 14, 745–754, doi:10.1175/1520-0450(1975)014<0745:FOG>2.0.CO;2, 1975.

Rogers, R. R. and Yau, M. K.: Short Course In Cloud Physics, 3rd Edn., Butterworth-Heinmann, 1989.

Rosenfeld, D.: Dynamic Characteristics of Cumuliform Clouds and Cloud Systems and their Influence on Rainfall, Ph.D., Atmospheric Sciences, Hebrew University, Jerusalem, 1986.

Saaroni, H., Halfon, N., Ziv, B., Alpert, P., and Kutiel, H.: Links between the rainfall regime in Israel and location and intensity of Cyprus lows, Int. J. Climatol., 30, 1014–1025,

doi:10.1002/joc.1912, 2010.

Saha, S., Moorthi, S., Pan, H.-L., Wu, X., Wang, J., Nadiga, S., Tripp, P., Kistler, R., Woollen, J., Behringer, D., Liu, H., Stokes, D., Grumbine, R., Gayno, G., Wang, J., Hou, Y.-T., Chuang, H.-Y., Juang, H.-M. H., Sela, J., Iredell, M., Treadon, R., Kleist, D., Van Delst, P., Keyser, D., Derber, J., Ek, M., Meng, J., Wei, H., Yang, R., Lord, S., Van Den Dool, H., Kumar, A., Wang, W., Long, C., Chelliah, M., Xue, Y., Huang, B., Schemm, J.-K., Ebisuzaki, W., Lin, R., Xie, P., Chen, M., Zhou, S., Higgins, W., Zou, C.-Z., Liu, Q., Chen, Y., Han, Y., Cucurull, L., Reynolds, R. W., Rutledge, G., and Goldberg, M.: The NCEP Climate Forecast System Reanalysis, B. Am. Meteorol. Soc., 91, 1015–1057, doi:10.1175/2010BAMS3001.1, 2010.

Schmidt, F. H.: An Elementary Theory of the Land and Sea Breeze Circulation, J. Meteorol., 4, 9–20, doi:10.1175/1520-0469(1947)004<0009:AETOTL>2.0.CO;2, 1947.

Schoenberger, L. M.: Doppler Radar Observation of a Land-Breeze Cold-Front, Mon. Weather Rev., 112, 2455–2464, 1984.

Shin, D. B., North, G. R., and Bowman, K. P.: A summary of reflectivity profiles from the first year of TRMM radar data, J. Climate, 13, 4072–4086, 2000.

Smith, R. B.: Mechanisms of Orographic Precipitation, Meteorol. Mag., 118, 85–88, 1989.

Smith, R. B.: Progress on the theory of orographic precipitation, Geological Society of America, Boulder, Colorado, 2006.

Stickley, A. R.: An Evaluation of the Bergeron-Findeisen Precipitation Theory, Mon. Weather Rev., 68, 272–280, doi:10.1175/1520-0493(1940)068<0272:AEOTBP>2.0.CO;2, 1940.

Trenberth, K. E., Fasullo, J. T., and Kiehl, J.: Earth's Global Energy Budget, B. Am. Meteorol. Soc., 90, 311–323, doi:10.1175/2008bams2634.1, 2009.

Wallace, J. M. and Hobbs, P. V.: Atmospheric Science, 2nd Edn., 383–391, 2006a.

Wallace, J. M. and Hobbs, P. V.: Atmospheric Science, 2nd Edn., 70 pp., 2006b.

Wang, J. and Wolff, D. B.: Comparisons of reflectivities from the TRMM precipitation radar and ground-based radars, J. Atmos. Ocean. Technol., 26, 857-875875, doi:10.1175/2008jtecha1175.1, 2009.

Wobus, H. B., Murray, F. W., and Koenig, L. R.: Calculation of the Terminal Velocity of Water Drops, J. Appl. Meteorol., 10, 751–754, doi:10.1175/1520-0450(1971)010<0751:COTTVO>2.0.CO; 2, 1971.

Wolff, D. B., Marks, D. A., Amitai, E., Silberstein, D. S., Fisher, B. L., Tokay, A., Wang, J., and Pippitt, J. L.: Ground Validation for the Tropical Rainfall Measuring Mission (TRMM), J. Atmos. Ocean. Technol., 22, 365–380, 2005.

Wolff, D. B. and Fisher, B. L.: Comparisons of instantaneous TRMM ground validation and satellite rain-rate estimates at different spatial scales, J. Appl. Meteorol. Climatol., 47, 2215–2237, doi:10.1175/2008jamc1875.1, 2008.

Yang, S. and Smith, E. A.: Mechanisms for diurnal variability of global tropical rainfall observed from TRMM, J. Climate, 19, 5190–5226, 2006.

Zangvil, A. and Druian, P.: Upper Air Trough Axis Orientation and the Spatial-Distribution of Rainfall over Israel, Int. J. Climatol., 10, 57–62, 1990.